# Novel nanoparticle CS-$C_{60}$-$Fe_3O_4$ magnetically induces tissue-specific aggregation and enhances thermal ablation of hepatocellular carcinoma

Jie Sun[1†], Zhengyao Chang[2†], Xudong Gao[3†], Huiwei Sun[4], Yantao Chai[5], Xiaojuan Li[4], Xiaoming Zhang[6] and Fan Feng[5*]

†Jie Sun, Zhengyao Chang and Xudong Gao equally contribute to this work.

*Correspondence:
fengfanbio@126.com

[1] Department of Oncology, Fifth Medical Center of Chinese PLA General Hospital, Beijing 100039, China
[2] Department of General Surgery, First Medical Center of Chinese PLA General Hospital, Beijing 100853, China
[3] Department of Hepatology, Fifth Medical Center of Chinese PLA General Hospital, Beijing 100039, China
[4] Institute of Infectious Diseases, Department of Infectious Diseases, Fifth Medical Center of Chinese PLA General Hospital, Beijing 100039, China
[5] Clinical Laboratory, The Fifth Medical Center, Chinese People's Liberation Army (PLA) General Hospital, Beijing 100039, China
[6] Graduate School of Chinese PLA General Hospital, Beijing 100853, China

## Abstract

Metallofullerenes are an important type of metallic nanomaterial with promising applications in several medical fields. Thermal ablation, including radiofrequency ablation (RFA) and microwave ablation (MWA), is an important treatment strategy for advanced hepatocellular carcinoma (HCC). The thermal expansion of fullerenes makes them good adjuncts to thermal ablation treatment of HCC. In this study, we used an innovative method of emulsification and cross-linking to produce CS-$C_{60}$-$Fe_3O_4$ (Chitosan-$C_{60}$-$Fe_3O_4$) nanoparticles, which have the advantages of uniform particle size and high bioavailability, as a kind of novel nano-pharmaceutical. The CS-$C_{60}$-$Fe_3O_4$ nanoparticles were prepared by the cross-linking reaction from chitosan–acetic acid solution, $Fe_3O_4$ nanoparticles by $Fe_2SO_4 \cdot 7H_2O$ and $FeCl_3 \cdot 6H_2O$, and $C_{60}$. The average particle size of CS-$C_{60}$-$Fe_3O_4$ was 194.3 nm. Because CS-$C_{60}$-$Fe_3O_4$ is magnetic, it can achieve specific and tissue aggregation in HCC tumor tissues. Moreover, compared with normal soluble $C_{60}$ (EL35-$C_{60}$), CS-$C_{60}$-$Fe_3O_4$ prolonged the retention time of $C_{60}$ in the blood of mice. CS-$C_{60}$-$Fe_3O_4$ alone is not cytotoxic to cultured cells or tumor tissues, but when combined with thermal ablation strategies (RFA and MWA), it significantly upregulates the antitumor effects of thermal ablation on HCC tissues, that is, it acts as a sensitiser to thermal ablation. In the presence of thermal ablation, CS-$C_{60}$-$Fe_3O_4$ interfered with iron metabolism in HCC cells and induced ferroptosis of HCC cells in the tumor tissues. These results not only expand our understanding of metallofullerenes but also provide additional options for the treatment of advanced HCC.

**Keywords:** Nano-pharmaceutical, Metallofullerenes, CS-$C_{60}$-$Fe_3O_4$, Hepatocellular carcinoma, Thermal ablation, Microwave ablation, Radiofrequency ablation

## Introduction

The most important risk factors for hepatocellular carcinoma (HCC) are various acute and chronic liver diseases caused by hepatitis viruses, such as HBV and HCV (Sung et al. 2021; The Polaris Observatory HCV Collaborators 2022; GBD 2019 Hepatitis B

Collaborators 2022). Despite the adoption of many measures (including universal and mandatory HBV vaccination of newborns, antiviral symptomatic treatment of HBV, etc.), more than 80 million people in China are currently infected with the hepatitis virus, which represents a serious public health challenge in China (Sung et al. 2021; The Polaris Observatory HCV Collaborators 2022; GBD 2019 Hepatitis B Collaborators 2022; Wang et al. 2014). Because most patients with HCC are initially diagnosed at an advanced stage (i.e., intermediate-to-advanced HCC, which is not suitable for surgical resection), localized treatments, such as various thermal ablation treatments (radiofrequency ablation or microwave therapy) are the most suitable treatments or primary treatment strategies for patients with advanced HCC (Forner et al. 2018). In the case of patients with advance HCC, thermal ablation is performed by percutaneous puncture guided by CT (computed tomography) or 3D colour ultrasound, allowing the treatment to be localized to the HCC tissue, thus avoiding damage to the normal liver tissue surrounding the HCC (Wang et al. 2022a). However, many challenges are associated with thermal ablation therapy, including incomplete ablation and the recurrence of HCC after ablation (Ikemoto et al. 2017). Therefore, it is important to develop safer and more effective thermal ablation treatments and combine them with other treatment strategies.

Fullerenes, which are enclosed spherical carbon monomers with a diameter of approximately 0.71 nm, contain carbon atoms on the surface of the molecule, which makes them highly reactive and easy to modify nanoparticles (Gallego et al. 2022; Tanzi et al. 2022). Clusters of metal atoms embedded in fullerene carbon cages form metal fullerenes which can be modified to achieve a certain degree of biomedical targeting (Liao et al. 2022). Moreover, targeted heat-treatment can induce phase transition and the expansion of fullerene nanoparticles while extravasating the tumor blood vessel. The explosive structural change of the fullerene nanoparticles has a devastating impact on abnormal tumor blood vessels, resulting in a rapid and extensive ischemia necrosis and shrinkage of the tumors (Li et al. 2022a). Metallofullerenes have advantages over conventional fullerenes, especially in terms of their magnetic properties, which allow them to be distributed in a directional manner under the influence of a magnetic field (Feng et al. 2018b). Thus, metallofullerenes are ideal combinations for precise HCC-related drug delivery and thermal ablation. However, existing metallofullerenes are mainly synthesised using various transition metals that are not sufficiently magnetic. In the present study, we prepared novel iron-metallofullerenes ($CS$-$C_{60}$-$Fe_3O_4$), which can achieve specific distribution in tumor tissue in the presence of a magnetic field. Metallofullerenes induce ferroptosis (the iron-dependent cell death) in HCC tissues and sensitise them to thermal ablation.

## Experimental section/methods

### Agents

Chitosan (CS) was obtained from Shanghai Crystal Pure Reagent Co., Ltd. Ferric chloride, ferrous sulphate, sodium hydroxide, and anhydrous ethanol were purchased from Sinopharm Chemical Reagent Co., Ltd. Span 80 and liquid paraffin were purchased from Chemical Pure Jiangsu Qiangsheng Functional Chemical Co. Ltd. Petroleum ether was purchased from Tianjin Fuyu Fine Chemical Co. Ltd. HCC cells were obtained from the National Infrastructure of Cell Line Resources, China Union Medical College, Chinese

Academy of Medical Sciences (Beijing, China). The cells, which were validated by STR, were cultured using DMEM supplemented with 10% FBS.

### Synthesis of CS-$C_{60}$-$Fe_3O_4$

$Fe_2SO_4 \cdot 7H_2O$ and $FeCl_3 \cdot 6H_2O$ were weighed in a molar ratio of 1:2 and dissolved in distilled water. Immediately after dissolution, the two solutions were transferred to a flask, the bottle stopper was quickly closed, and $N_2$ was added to remove air from the flask. The mixture was then stirred rapidly. Under continuous supply of $N_2$, the ammonia solution was slowly added dropwise to the mixed iron ion solution; the mixed solution first turned yellow and then slowly turned black. The pH of the system was determined using pH test paper. When the pH reached 11, the dropwise addition of the ammonia solution was stopped. Lastly, the obtained black ferric oxide particles were magnetized on the bottom of a Petri dish, washed several times with absolute ethanol and distilled water, and freeze-dried to obtain $Fe_3O_4$ nanoparticles.

The chitosan powder was then weighed and dissolved in a 2% acetic acid solution in a constant-temperature magnetic stirrer at room temperature until the powder was complete dissolution. The resulting chitosan–acetic acid solution was the sonicated. Simultaneously, paraffin and emulsifier Span 80 was added to the flask, and the mixture was stirred, and mixed evenly, after which $Fe_3O_4$ magnetic powder was added and mixed for 15 min and the mixture ultrasonicated into the oil phase. Mechanical stirring was continued for 15 min to further disperse uniformly. The mixture was then heated to 60 ℃, and 2 mL of 25% wt glutaraldehyde solution was added, the cross-linking reaction was carried out for 2 h. After the reaction was complete, the mixture was transferred to a Petri dish and washed three times with isopropanol and petroleum ether under magnetic adsorption conditions. Black magnetic chitosan microspheres were also obtained. The obtained CS-$Fe_3O_4$ and $C_{60}$ were added to a 60-mL water flask at a ratio of 3:1, after which 10 g NaOH was added, and the mixture stirred at 70 ℃ for 48 h. In the last step, the solution was dialyzed with ultrapure water to obtain CS-$C_{60}$-$Fe_3O_4$. The synthesis route to obtain CS-$C_{60}$-$Fe_3O_4$ is shown in Fig. 1A.

### Fourier transform infrared spectroscopy

The Fourier transform infrared spectrometry (FTIR), which based on the principle of light coherence, is an effective means of identifying and analyzing substances. Depending on the wavelength range, infrared light can be divided into three wave regions: infrared, mid-infrared, and far-infrared region (2.5–25 μm; 4000–400 cm$^{-1}$) can be used to investigate various physical processes and molecular structure characteristics within the molecule and is thus an effective tool for solving various problems in molecular structure and chemical composition. The lyophilized samples were rendered into transparent flakes using the KBr tableting method. The sheet was gently placed in a sample holder and inserted into the sample cell. The infrared spectra in the mode and parameters set by the software were tested. The empty light background signal was scanned, the sample signal was scanned, and the infrared spectrum of the sample was obtained after the Fourier transform. After dissolving CS-$C_{60}$-$Fe_3O_4$ in water, the concentration of $C_{60}$ in the solution can reach more than 4 mg/ml.
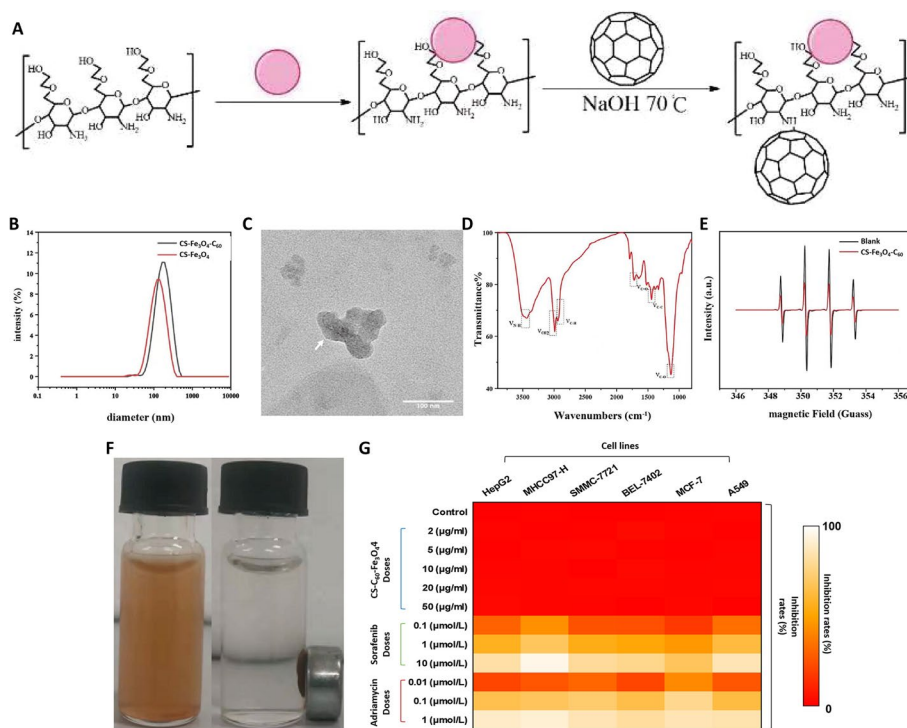
**Fig. 1** Preparation and characterization of CS-C$_{60}$-Fe$_3$O$_4$. **A** Basic synthetic route of CS-C$_{60}$-Fe$_3$O$_4$ in the present study. Schematic diagrams of the synthesis of CS-C$_{60}$-Fe$_3$O$_4$ (the pink ball represents Fe$_3$O$_4$, the chemical structure of the polymer chitosan and the structure of fullerene C$_{60}$ are also illustrated). **B** Hydrodynamic size distribution of CS-C$_{60}$-Fe$_3$O$_4$ by dynamic light scattering (DLS). **C** Transmission electron microscopy (TEM) images of CS-C$_{60}$-Fe$_3$O4. **D** Fourier transform infrared (FT-IR) spectrum of CS-C$_{60}$-Fe$_3$O$_4$. (E) Electron paramagnetic resonance (EPR) spectra of •OH captured by DMPO. **F** Separation of CS-C$_{60}$-Fe$_3$O$_4$ nanoparticles by magnetic effect. **G** Inhibition rates of CS-C$_{60}$-Fe$_3$O$_4$ and other agents on cell lines. The results were shown as heat-map image (**G**)

## Hydrated particle size analysis

Dynamic Light Scattering (DLS), also known as Photon Correlation Spectroscopy (PCS) or quasi-elastic scattering, measures fluctuations in light intensity over time. DLS technology for measuring particle size has the advantages of accuracy, rapidity, and good repeatability, and has become a relatively conventional characterization method in nanotechnology. The DLS instrument used in this study not only measures particle size, but also has the ability to measure zeta potential. Therefore, it is widely used to describe a wide variety of particulate systems, including synthetic polymers, oil-in-water emulsions, water-in-oil emulsions, vesicles, micelles, biological macromolecules, pigments, dyes, silica, metal sols, ceramics, and other colloidal suspensions and dispersions. To determine the particle size of the samples, an appropriate amount of the sample was diluted with ultrapure water, and the mixture was ultrasonically treated for 30 min and then filtered through a water-based needle filter with a pore size of 0.22 μm. A Beckman coulter N$_5$ laser particle sizer was used to measure particle size and distribution.

## In vitro elimination of hydroxyl radicals

Electron paramagnetic resonance (EPR) is a magnetic resonance technique that originates from the magnetic moments of unpaired electrons. In the case of free radicals,

the orbital magnetic moment has little effect and the vast majority (> 99%) of the total magnetic moment originates from the electron spin. EPR was used to test the ability of $CS$-$C_{60}$-$Fe_3O_4$ to scavenge free radicals and produce hydroxyl radicals, 100 μL of DMPO (100 mM), 50 μL of $H_2O_2$ (1 mol/L), and 50 μL of ultrapure water were mixed with $CS$-$C_{60}$-$Fe_3O_4$, and the mixture was illuminated with 500 W UV light for 4 min to detect the hydroxyl free base signal.

### Cytotoxicity testing of $CS$-$C_{60}$-$Fe_3O_4$

The Cytotoxicity of $CS$-$C_{60}$-$Fe_3O_4$ was examined using in vitro and in vivo assays. The cell lines (including HCC cell lines (HepG2, MHCC97-H, BEL-7402, and SMMC-7721), the breast cancer cell line MCF-7, and non-small cell lung cancer cell line A549) were cultured in high glucose DMEM solution containing 10% FBS and 1% penicillin–streptomycin dual antibody solution (temperature: 37 °C; $CO_2$ concentration: 5%). These cell cultures were seeded into 96-well plates at a density of $5 \times 10^4/cm^2$, and, after 24 h in the incubator, the medium was replaced with DMEM medium at different concentrations (2, 5, 10, 20, 50 μg/mL) of $CS$-$C_{60}$-$Fe_3O_4$. After another 24 h of incubation, the old medium was removed, and 10 μL of CCK-8 and 100 μL of colourless DMEM were added to each well for approximately 1 h, at which point the absorbance at 450 nm (as an indicator of cell viability) was measured with a microplate reader (Hao et al. 2023). During the cell culture experiments, the TKI (tyrosine kinase inhibitor) sorafenib and cytotoxic chemotherapeutic drug adriamycin were used as positive controls. DMSO was used to configure the drug to be used, and DMEM without FBS was used to dilute the drug (Wang et al. 2021), with doses of 10, 1, and 0.1 μmol/L for sorafenib; and 1, 0.1, and 0.01 μmol/L for adriamycin. The inhibitory rates of $CS$-$C_{60}$-$Fe_3O_4$, sorafenib, and Adriamycin on the cells were calculated according to the optical density at 450 nm and are shown as heat-map images (Huo et al. 2019). For in vivo assays, MHCC97-H cells were cultured and prepared as single-cell suspension (Hao et al. 2023; Wang et al. 2021; Huo et al. 2019). Next, the single-cell suspension was injected subcutaneously into nude mice to form subcutaneous tumor tissues. $CS$-$C_{60}$-$Fe_3O_4$ was administered via tail vein injection (Hao et al. 2023; Wang et al. 2021; Huo et al. 2019). The protocol was as follows: starting one week after cell inoculation of nude mice, each animal was injected once a week at a dose of 40 mg/kg for 5–6 weeks, after which the animals were euthanized, and tumor volume, tumor weight, animal body weight, and weight of major organs was measured, and blood tests were performed in the control group (untreated group) and the $CS$-$C_{60}$-$Fe_3O_4$ group, respectively (Ma et al. 2022a).

### Transmission electron microscopy sample analysis

Transmission electron microscopy (TEM) is a useful tool in the fields of materials, physics, chemistry, and life sciences to obtain information on the surface (or topography) and interior of samples. The basic principle is that an accelerated and concentrated electron beam is used to irradiate nanoparticles, and the electrons collide with the courtyard in the nanoparticles, thereby changing their direction. The electronic image was converted into a visible-light image, showing the morphology and structure of the particles. A Tecnai G2 F20 field-emission transmission electron microscope was used to analyse the morphology and size of the samples. A small amount of lyophilised $CS$-$C_{60}$-$Fe_3O_4$,

mixed in alcohol and sonicated for 30 min to fully disperse it. The sample was dropped onto a microgrid and observed with a transmission electron microscope after drying.

### In vivo tumor model of hepatocellular carcinoma

In the present study, nude mice (thymus-deficient immunodeficient BALB/c mice), 4–6 weeks old, were purchased from Si-Bei-Fu Corporation, Beijing, China. MHCC97-H cells were cultured and single-cell suspensions were prepared. The single-cell suspension was directly injected subcutaneously into nude mice to form tumor tissues (Wang and Wang 2019).

#### *The soluble fullerene control*

The fullerene powder ($C_{60}$) is mixed and dissolved using toluene, after which EL-35 is slowly added and, after thorough mixing, the toluene is evaporated from the mixture by vacuum lyophilisation. Water-soluble fullerenes were obtained by dilution with sterile saline. This soluble fullerene control, named as EL35-$C_{60}$, has a fullerene content of up to approximately 0.5 mg/mL (the final concentration of EL-35 does not exceed 2%).

#### *The tissue-distribution of CS-$C_{60}$-$Fe_3O_4$*

When the HCC cells formed subcutaneous tumor tissues and the tumor volume reached 1500–2000 $m^3$, the mice received CS-$C_{60}$-$Fe_3O_4$ or the Soluble Fullerene control (EL35-$C_{60}$) via tail vein injection at a dose of 40 mg/kg. Tumor tissues were treated with ultra-strong magnets to enable CS-$C_{60}$-$Fe_3O_4$ to enrich and aggregate in the subcutaneous tumor tissue. The tissue samples are being taken from the same living mice at each of these three time points (0-time point, 8 h time point and 24 h time point): the mice are sorted into three groups, to be euthanized at 0, 8, or 24 h and the tissues from the killed animals excised. A precision balance was used to divide and obtain approximately 50 mg of various organs or tissues in which to assay for $C_{60}$ content. The total amount of $C_{60}$ in each animal was determined from the animal's body weight/organ weights and the dose of $C_{60}$ (40 mg/kg) and plotted in R. The distribution density of fullerenes in each major organ and tissue ($C_{60}$ per 50 mg of tissue) was also tabulated (Wang et al. 2022b; Wang et al. 2022c; Xie et al. 2018).

#### *The thermal ablation on HCC tissues*

MHCC97-H cells were cultured and injected into nude mice to generate subcutaneous tumor tissues. CS-$C_{60}$-$Fe_3O_4$ was administered via tail vein injection, and super-strong magnets were applied to the subcutaneous tumor surface to enable CS-$C_{60}$-$Fe_3O_4$ to be enriched and distributed in the tumor tissue. A thermal ablation experiment is first performed, where the subcutaneous tumor tissue is subjected to RFA (60 ℃ for 2 min, 55 ℃ for 2 min or 50 ℃ for 2 min) or MWA (55 ℃ for 2 min, 50 ℃ for 2 min or 45 ℃ for 2 min) to determine the specific conditions for thermal ablation (Wang et al. 2021; Shao et al. 2018; Ma et al. 2020). The three modes of treatment in the animals were: drug administration alone, thermal ablation alone, and drug administration plus thermal ablation. The volume of tumor tissue was measured every 7 days, and when the tumor volume reached 1,800–2,000 mm3, the next experimental steps were performed. A 40 mg/kg dose of CS-$C_{60}$-$Fe_3O_4$ was injected through the tail vein, after which a super magnet

was adhered to the subcutaneous tumor site for approximately 24 h. MWA or RFA was performed by direct percutaneous puncture of the tumor tissues (Wang et al. 2021; Shao et al. 2018; Ma et al. 2020). After thermal ablation was completed, tumor volume was measured every seven days to plot the tumor growth curve (Wang et al. 2021; Shao et al. 2018; Ma et al. 2020). Lastly, the animals were euthanized and the tumor tissue was collected, photographed, and weighed.

### Ferroptosis detection

The relative concentration of MDA in subcutaneous tumor tissue lysates was assessed using an MDA Assay Kit (ab118970; Abcam), according to the manufacturer's instructions. (Li et al. 2022b; Rathmell et al. 2022) This assay measures the reaction of MDA with thiobarbituric acid (TBA), which generates an MDA-TBA adduct which can be quantified colourimetrically (OD $= 532$ nm). A Lipid Peroxidation (4-HNE) Assay Kit (ab238538; Abcam) was used to evaluate the concentration of 4-HNE in HCC tumor tissues via immunohistochemistry according to the manufacturer's protocol to measure Ferroptosis of HCC tumors (Li et al. 2022b; Rathmell et al. 2022). The expression levels of ferroptosis-related factors, including transferrin receptor 1 (TFR1), arachidonic acid 15-lipoxygenase-1 (ALOX15), and glutathione peroxidase 4 (GPX4), in subcutaneous tumor tissues were measured by western blotting (Li et al. 2022b; Rathmell et al. 2022).

### Statistical analysis

All statistical analyses were performed using GraphPad 8.0 (GraphPad Software Corporation, Armonk, NY, USA). A P value $< 0.05$ indicates that there is a statistically significant difference between the two datasets. The main comparison in this study was between multiple experimental groups. Ordinary one-way analysis of variance (ANOVA) and multiple comparison methods were used for multi-grouped data. An analysis of variance (ANOVA) was used to examine whether any differences between the groups could be detected. Multiple comparisons (t-tests) were used to detect the differences between pairs of data.

## Results

### Preparation and characterization of CS-$C_{60}$-$Fe_3O_4$

We prepared CS-$C_{60}$-$Fe_3O_4$ by emulsification and crosslinking and characterised it accordingly. An appropriate amount of the sample was diluted with ultrapure water, ultrasonically treated for 30 min, and filtered through a water-based needle filter with a pore size of 0.22 μm. The average moisture and particle size of CS-$Fe_3O_4$ measured using a dynamic light scattering particle size analyser (DLS) were 128.9 nm, and the average moisture and particle size increased to 194.3 nm after the incorporation of $C_{60}$ (Fig. 1B). This is slightly larger than the TEM result (Fig. 1C), which may be due to the hydrated particle size of the sample measured by DLS.

Through analysis of the infrared spectrum obtained by Fourier transform infrared absorption spectroscopy (FT-IR), it can be seen that the absorption peak at 3450 cm$^{-1}$ is the common absorption peak of -NH and -OH due to hydrogen bond interactions, and the peak at 2900 cm$^{-1}$ and it belongs to the stretching vibration absorption peak of C-H (Fig. 1D). The peaks at 1,600 cm$^{-1}$ belong to the amide I band of chitosan, 1450 and

$1100 \text{ cm}^{-1}$ belong to C–C and C–O, respectively (Fig. 1D). This indicated that $C_{60}$ was successfully synthesised using chitosan. Thermogravimetric analysis of lyophilised CS-$C_{60}$-Fe$_3$O$_4$. We therefore tested the ability of CS-$C_{60}$-Fe$_3$O$_4$ to scavenge OH by electron paramagnetic resonance (EPR) in vitro, as can be seen from Fig. 1E, the radical scavenging efficiency of CS-$C_{60}$-Fe$_3$O$_4$ nanoparticles at 100 μg/mL is approximately 65%. Further, we examined the FTIR spectrum characteristics of CS and $C_{60}$ mixtures. The results showed that the FTIR spectrum profile of the CS-$C_{60}$ simple mixture (Additional file 1: Fig. S1) was extremely different from that of CS-$C_{60}$-Fe$_3$O$_4$ (Fig. 1D), thus this further supports the idea that the CS-$C_{60}$-Fe$_3$O$_4$ nanoparticle is a combination of the three components that are linked together to form a whole rather than a simple mixture.

**Magnetic field-induced recruitment and tissue distribution of CS-$C_{60}$-Fe$_3$O$_4$**

The magnetic properties of CS-$C_{60}$-Fe$_3$O$_4$ were further tested. The results are shown in Fig. 1F: CS-$C_{60}$-Fe$_3$O$_4$ was dispersed in water to form a reddish-brown liquid, and under the action of a strong magnet, CS-$C_{60}$-Fe$_3$O$_4$ in water was able to be almost completely adsorbed to the magnet. At this point the CS-$C_{60}$-Fe$_3$O$_4$ was separated out of the solution and the liquid becomes colourless and transparent again.

Next, the in vivo effect of CS-$C_{60}$-Fe$_3$O$_4$ on the tissue distribution of fullerenes in mice was further examined to determine whether enrichment in tumor tissues could be achieved. As can be seen in Figs. 2, 3, Table 1 and Additional file 3: Table S1, there was no significant difference in tissue distribution between EL35-$C_{60}$ (a soluble fullerene formulation as control) and CS-$C_{60}$-Fe$_3$O$_4$ in mice under non-magnetic field conditions at 0-time point. At the 0-time point, $C_{60}$ is predominantly distributed in the blood (up to 25 μg [$25.29 \pm 2.88$ μg] of $C_{60}$ per 50 μL blood sample), but, over time, $C_{60}$ is rapidly transferred from the blood to the internal organs ($C_{60}$ was only $0.77 \pm 0.09$ μg/50 μL in the blood at the 8-h timepoint and was largely undetectable in the blood at the 24-h
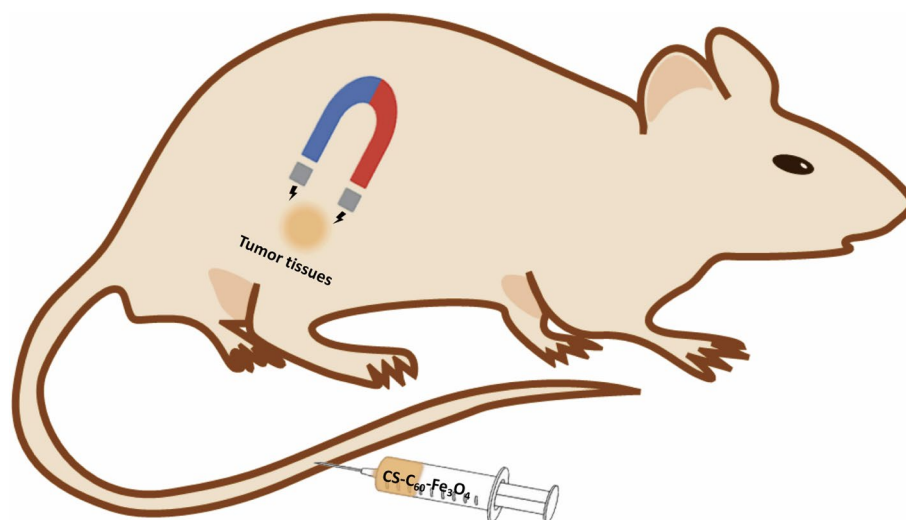


**Fig. 2** Aggregation of CS-$C_{60}$-Fe$_3$O$_4$ in subcutaneous tumor tissue induced by magnetic fields. MHCC97-H cells were obtained in culture, after which MHCC97-H cells were inoculated with nude mice to obtain subcutaneous tumor tissue. CS-$C_{60}$-Fe$_3$O$_4$ was administered to the experimental animals by tail vein injection. Adhesion to the surface of subcutaneous tumor tissue in nude mice was used to induce enrichment of CS-$C_{60}$-Fe$_3$O$_4$ in subcutaneous tumor tissue
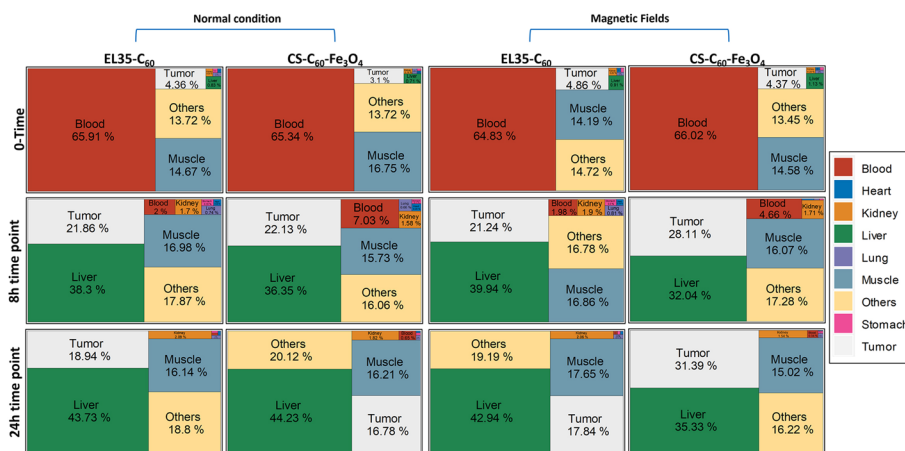
**Fig. 3** Tissue distribution of EL35-$C_{60}$ and CS-$C_{60}$-$Fe_3O_4$ in nude mice under different conditions. After obtaining MHCC97-H cells in culture, the cells were inoculated into nude mice to form subcutaneous tumor tissues. Thereafter, half of the animals had supermagnets attached to the tumor tissue, while the other half did not have magnets attached. The animals were collected at different time points and the $C_{60}$ content of each type of tissue and organ was assayed to determine the final distribution of $C_{60}$ in the organs and tissues of nude mice under different conditions based on organ weight and $C_{60}$ content. The legend shows the main organs or tissues, where others represent the amount of $C_{60}$ in the spleen, brain, bone, and other tissues and organs as well as the amount of $C_{60}$ metabolised

time-point [$C_{60}$ concentrations were as low as 0.02 μg/50 μL, 0.02 ± 0.00 μg/50 μL]). In contrast, the preparation of fullerenes as CS-$C_{60}$-$Fe_3O_4$ was able to prolong the presence of $C_{60}$ in the blood; for example, at the 8-h time-point, $C_{60}$ levels in the blood of the CS-$C_{60}$-$Fe_3O_4$ group of mice reached 2.7 μg/50 μL [2.71 ± 0.36] and were still as high as 0.26 ± 0.02 μg/50 μL at the 24-h time-point. When comparing these tissues and organs cross-sectionally, $C_{60}$ gradually centralised to the liver over time, and its distribution in the liver (the distribution of $C_{60}$ in the liver tissue exceeded 20 μg/50 mg [20.8 ± 3.49 μg/50 mg for EL35-$C_{60}$ or 21.2 ± 2.53 μg/50 mg for CS-$C_{60}$-$Fe_3O_4$ at 8 h time point; 24.0 ± 3.29 μg/50 mg for EL35-$C_{60}$ or 25.7 ± 3.86 μg/50 mg for CS-$C_{60}$-$Fe_3O_4$ at 24 h time point]) was significantly higher than that in other organs or tissues.

Next, the magnetic field did not affect the tissue distribution of EL35-$C_{60}$, but significantly induced the distribution of CS-$C_{60}$-$Fe_3O_4$ in tumor tissue (Figs. 2, 3, Table 1 and Additional file 3: Table S1): $C_{60}$ levels in tumor tissue increased from 0.09 ± 0.00, 0.64 ± 0.06, and 0.47 ± 0.05 μg/50 mg to 0.13 ± 0.02, 0.80 ± 0.08 and 0.90 ± 0.13 μg/50 mg at 0, 8, and 24 h, respectively. The tissue distribution of $C_{60}$ under different conditions was also calculated by combining the weights of different organs and tissues. The results are shown in the Fig. 3: where $C_{60}$ in the blood is reduced from over 65% (66.14 ± 6.13%) at the 0 h time-point to less than 1% (0.07 ± 0.00) at 24 h, whereas $C_{60}$ in the liver accounted for the majority of the total $C_{60}$ in the mouse (able to reach approximately 40%: [38.40 ± 3.04%] at the 8-h time point and [43.85 ± 3.20%] at 24-h time point). In addition, CS-$C_{60}$-$Fe_3O_4$ prolonged the presence of $C_{60}$ in the blood (approximately 7% [7.05 ± 0.60%] of the $C_{60}$ weight in the tissues at 8 h). The tissue distribution of $C_{60}$ in the EL35-$C_{60}$ group did not change significantly under the influence of the magnetic field. However, the distribution of $C_{60}$ in the tumor tissue was significantly enhanced in the CS-$C_{60}$-$Fe_3O_4$ group (from 21.32 ± 2.16% to 28.23 ± 3.10% at 8 h time point and from 17.92 ± 1.77% to 31.21 ± 2.91% at 24 h time point). Moreover, the corresponding

**Table 1** Values of the Parameters of each group of nude mice after tail vein injection of CS-$C_{60}$-$Fe_3O_4$

| Parameters | Control | CS-$C_{60}$-$Fe_3O_4$ concentration (mg/kg) | | | |
|---|---|---|---|---|---|
| | | 10 | 20 | 30 | 40 |
| Body weight (g) | 19.56 ± 0.76 | 19.53 ± 0.78 | 19.43 ± 0.77 | 19.42 ± 0.80 | 19.58 ± 0.86 |
| Heart (mg) | 103.18 ± 16.09 | 107.06 ± 8.22 | 104.73 ± 7.61 | 103.10 ± 9.09 | 102.62 ± 7.19 |
| Lung (mg) | 142.99 ± 10.31 | 142.18 ± 9.46 | 140.05 ± 8.21 | 141.21 ± 13.51 | 141.15 ± 9.25 |
| Liver (mg) | 643.00 ± 18.10 | 648.53 ± 29.61 | 644.98 ± 21.48 | 643.55 ± 23.51 | 645.80 ± 26.74 |
| Stomach (mg) | 129.82 ± 10.48 | 126.39 ± 9.28 | 126.25 ± 6.33 | 125.26 ± 8.21 | 126.21 ± 7.89 |
| Double kidney (mg) | 231.71 ± 12.41 | 232.28 ± 12.70 | 231.01 ± 6.02 | 231.57 ± 18.79 | 232.17 ± 10.70 |
| Leukocyte($10^9$/L) | 3.39 ± 0.64 | 3.36 ± 0.55 | 3.31 ± 0.51 | 3.29 ± 0.53 | 3.41 ± 0.61 |
| Red blood cell($10^{12}$/L) | 9.29 ± 0.48 | 9.27 ± 0.39 | 9.33 ± 0.66 | 9.31 ± 0.62 | 9.31 ± 0.46 |
| Hemoglobin(g/L) | 152.51 ± 8.42 | 151.79 ± 4.74 | 151.64 ± 6.68 | 152.74 ± 5.74 | 151.51 ± 4.93 |
| Platelet count($10^9$/L) | 624.10 ± 16.63 | 628.46 ± 11.47 | 628.43 ± 9.02 | 623.93 ± 16.49 | 628.50 ± 13.40 |

The nude mice with subcutaneous tumor tissues were received CS-$C_{60}$-$Fe_3O_4$ via tail-vein injection

The animal weights, weights of major organs and major blood tests were examined

total Next, the stability assay of CS-$C_{60}$-$Fe_3O_4$ in rat serum was examined. A sample of 0.5 mg/ml (0-time point) by mixing CS-$C_{60}$-$Fe_3O_4$ with rat serum and the samples were incubated for 24 h (24 h-time point). As shown in Additional file 2: Fig. S2, incubation of CS-$C_{60}$-$Fe_3O_4$ samples at 37 °C for 24 h did not affect the absorption characteristics of CS-$C_{60}$-$Fe_3O_4$ samples. This indicates that the stability of CS-$C_{60}$-$Fe_3O_4$ in the presence of the blood circulatory system for 24 h is assured.

**The in vitro and in vivo toxicity of CS-$C_{60}$-$Fe_3O_4$ on HCC cells**

Next, the toxicity of CS-$C_{60}$-$Fe_3O_4$ on HCC cells and other cell lines was examined. First, the toxicity of CS-$C_{60}$-$Fe_3O_4$ on cultured cell lines was measured using the MTT assay. As shown in Fig. 1G, none of the five doses of CS-$C_{60}$-$Fe_3O_4$ was cytotoxic to liver-derived cells ( HepG2, MHCC97-H, MHCC97-L, BEL-7402, and SMMC-7721 cells), and CS-$C_{60}$-$Fe_3O_4$ was not cytotoxic to other selected tumor cell lines of different types and origins (including lung cancer cells A549, breast cancer cells MCF-7, lung cancer cells A549). As an important control, sorafenib, a typical TKIs used in advanced HCC, and adriamycin, a typical cytotoxic chemotherapy, have significant toxicity in these cells, and sorafenib and adriamycin were both found to inhibit the survival of these cells in a dose-dependent manner (Fig. 1G).

Next, the effect of CS-$C_{60}$-$Fe_3O_4$ was confirmed by using an in vivo model. MHCC97-H cells formed subcutaneous tumor tissues in nude mice. As shown in Fig. 4, tail-vein injection of CS-$C_{60}$-$Fe_3O_4$ did not modulate the volume or weight of tumors tissues formed by MHCC97-H cells in nude mice. At the same time, none of these doses of CS-$C_{60}$-$Fe_3O_4$ affected the weight of the major organs (Heart, Lung, Liver, Stomach or Double kidney), body weight and the main blood parameters (Leukocyte, Red blood cell, Hemoglobin or Platelet count) of the nude mice (Table 1). Therefore, the CS-$C_{60}$-$Fe_3O_4$ has good safety and did not exhibit significant toxicity in vitro or in vivo.

### Thermal ablation of HCC in a nude rat subcutaneous tumor model and selection of thermal ablation conditions

MHCC97-H cells were cultured and subcutaneously inoculated into nude mice to form tumors. After the volumes of the subcutaneous tumors reached 1,800–2,000 mm$^3$, the HCC tumors were treated with RFA or MWA under different conditions, and the results showed that the higher the temperature of RFA or MWA, the stronger the anti-tumor effect (Fig. 5). RFA treatment at 50 °C for 2 min and microwave ablation at 45 °C for 2 min did not result in significant antitumor effect and were chosen to simulate incomplete ablation in further experiments (Fig. 5).

### Sensitizing effect of CS-C$_{60}$-Fe$_3$O$_4$ on the thermal ablation of HCC

The combined effects of CS-C$_{60}$-Fe$_3$O$_4$ and incomplete thermal ablation on HCC were examined. As shown in Fig. 6, MHCC97-H cells were inoculated into nude mice to form subcutaneous tumor tissue, after which neither tail vein injection of CS-C$_{60}$-Fe$_3$O$_4$ nor incomplete thermal ablation [including the incomplete RFA (Fig. 6A) or MWA (Fig. 6B)] alone significantly affected the subcutaneous growth of MHCC97-H cells in nude mice, whereas [including the incomplete RFA (Fig. 6A) or MWA (Fig. 6B)] combined with CS-C$_{60}$-Fe$_3$O$_4$ significantly inhibited the subcutaneous growth of MHCC97-H cells in nude mice: this is reflected in the fact that the aforementioned incomplete ablation of HCC subcutaneous tumor tissue did not have a significant effect on tumor growth; however, incomplete ablation of HCC tissue after induction of CS-C$_{60}$-Fe$_3$O$_4$ using a magnetic field was able to inhibit the growth of HCC tissue (HCC tumor tissue growth stalled and shrank to a certain extent at the end of the experimental cycle).

Next, the potential mechanism of CS-C$_{60}$-Fe$_3$O$_4$ on the growth of HCC cells in vivo was examined. As shown in Fig. 6, the lipid peroxide 4-HNE-stained immunohistochemical sections of tumors indicated ferroptosis in HCC tumors. Compared with the control group, RFA, MWA, or CS-C$_{60}$-Fe$_3$O$_4$ alone did not induce ferroptosis in HCC cells in the tumor tissues; these did not affect the lipid peroxide 4-HNE level (Fig. 6). The combination of [including the incomplete RFA (Fig. 6A) or MWA (Fig. 6B)] with CS-C$_{60}$-Fe$_3$O$_4$ or MWA with CS-C$_{60}$-Fe$_3$O$_4$ induced ferroptosis in HCC cells in tumor tissues, enhancing lipid peroxide 4-HNE levels. Moreover, only the combination of RFA with CS-C$_{60}$-Fe$_3$O$_4$ or MWA with CS-C$_{60}$-Fe$_3$O$_4$ significantly increased MDA production in the tumor tissues, which confirmed their profound inhibitory effect on HCC tumor growth via the induction of ferroptosis (Fig. 6).

## Discussion

Solid tumors possess unique pathophysiological vasculatures that are not found in normal tissues or organs, including hypervasculature, defective vascular architecture, lack of lymphatic drainage, and extensive production of several permeability mediators (Laface et al. 2022; Ye et al. 2021). Fullerenes have good physicochemical properties and are widely used in the fields of photoelectric conversion, nanomaterials, and electronic informatics; however, they are also important therapeutic strategies for anti-tumor research (Zhao et al. 2023) and could be used as reliable antitumor agents for disrupting tumor vasculature and damaging tumor tissue owing to their thermal expansion
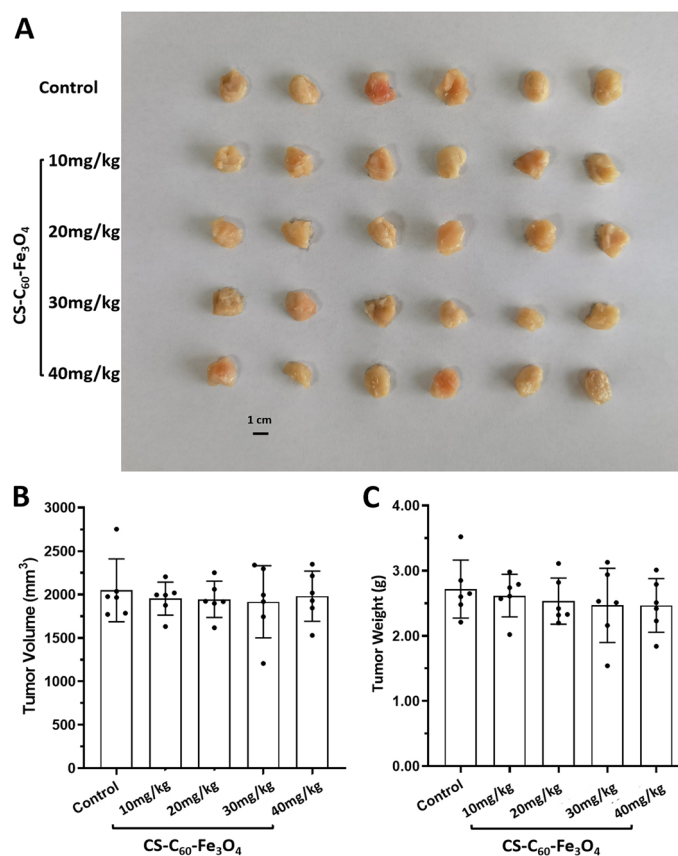
**Fig. 4** The in vivo toxicity of CS-C$_{60}$-Fe$_3$O$_4$ in nude mice model. The MHCC97-H cells were cultured and injected into the nude mice to form the subcutaneous tumor model. The CS-C$_{60}$-Fe$_3$O$_4$ was injected into nude mice via tail-vein. The results were shown as images of tumor tissues: **A** tumor volumes, **B** tumor weights, **C** *P < 0.05

properties (Li et al. 2022a; Feng et al. 2018b). In this study, we developed a novel soluble metallofullerene, CS-C$_{60}$-Fe$_3$O$_4$, which has many original features and significant potential for application in materials science. First, chitosan is a class of non-toxic and non-hazardous bioactive materials with excellent physicochemical properties, having an amino group at one end and easily reacting with fullerene and hydroxyl group at the other end, enabling complexation with Fe$_3$O$_4$ (as shown in this study) and the formation of an ideal bridge. Secondly, because fullerenes are normally insoluble in water, improving the preparation of soluble fullerenes has been the focus of recent research. In our study we prepared a soluble metallofullerene, CS-C$_{60}$-Fe$_3$O$_4$, whose solubility in water is as high as 20 mg/mL. Fe$_3$O$_4$ is also insoluble in water and can be stably dispersed in water after complexation with CS. Thirdly, conventional metallofullerenes require difficult methods and harsh conditions for preparation (formation of metallofullerene from oxides of transition elements and fullerenes by arcing in argon), requiring the use of graphene to form carbon nanocages under even harsher conditions to form metallofullerenes (Zheng et al. 2022). This high cost limits the applications of metal fullerenes. The development of novel fullerenes, such as CS-C$_{60}$-Fe$_3$O$_4$ in this study, greatly reduces the difficulty of preparing metallofullerenes, and iron-fullerenes are much less expensive in terms of material cost than transition-element/rare-earth element fullerenes. Of particular
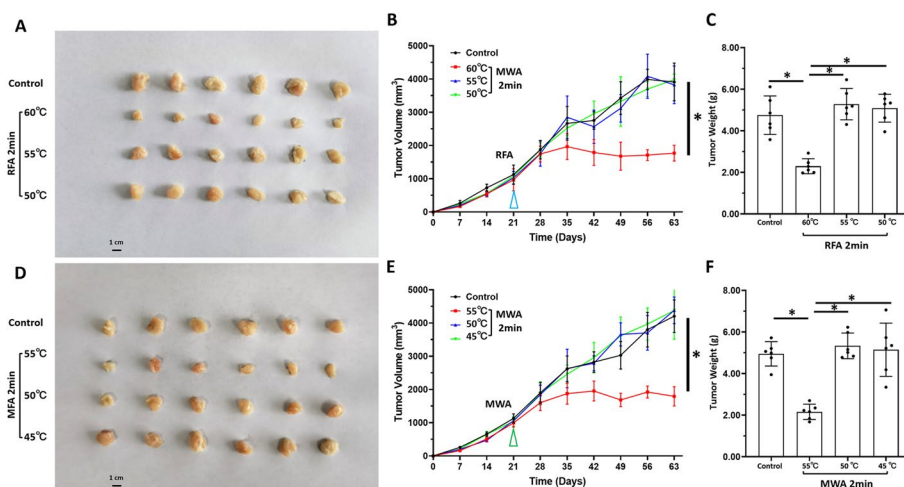
**Fig. 5** Selection of experimental conditions for thermal ablation. MHCC97-H cells were cultured and inoculated into nude mice to form subcutaneous tumors, after which the subcutaneous tumor tissue was treated with radiofrequency ablation (RFA) (**A**–**C**) and microwave ablation (MWA) (**D**–**F**). Tumor volumes were measured weekly to plot tumor growth curves, and tumor tissues were collected from the animals at the end of the experiment to weigh the tumors. *$P < 0.05$

importance is the fact that transition-element metal fullerenes are magnetic and have applications in the field of nuclear magnetic resonance. However, such magnetic properties are not comparable to those of iron (enrichment in specific tissues induced by magnetic fields). Therefore, this study represents a major innovation and breakthrough in fullerene-related research.

The metallofullerene has been considered as a kind of molecule composed of a metal atom (various Fe and transition metal elements) trapped inside into a fullerene carbon-cage and these metal atom(s) are encapsulated rather than being chemically bonded (Yamamoto et al. 1994; Funasaka et al. 1995). In the presence work, the $Fe_3O_4$ nanoparticle chemically or physically bonded on fullerene $C_{60}$ was not same as the definition of current metallofullerene and could not be named as "metallofullerene". Morepver, the magnetic feature of $La@C_{82}$ and $Gd@C_{82}$, two typical kinds of metallofullerene obtained from toluene solution, have been reported previously by Yamamoto et al. 1

994 and Funasaka et al. 1995; and the magnetic properties of these two kinds of metallofullerene could be examined by using the SQUID magnetometer (Yamamoto et al. 1994; Funasaka et al. 1995). According to these references, therefore in this nanostructure ($CS$-$C_{60}$-$Fe_3O_4$), the most of magnetization property of $CS$-$C_{60}$-$Fe_3O_4$ is related to $Fe_3O_4$ nanoparticles. These two are the biggest differences between $CS$-$C_{60}$-$Fe_3O_4$ and existing metal fullerene magnetic materials in this study.

The thermal ablation strategies, RFA or MWA, are the most commonly used local treatment strategies for advanced HCC and representative interventional strategies for advanced HCC (Wang et al. 2022a; Ikemoto et al. 2017). Although thermal ablation strategies can be applied directly to HCC tissue through percutaneous puncture guided by medical imaging, such as CT, to minimise the impact on the surrounding normal tissue, there are still many challenges associated with thermal ablation, including the ease with which patients can relapse after incomplete ablation (i.e. disease progression again after
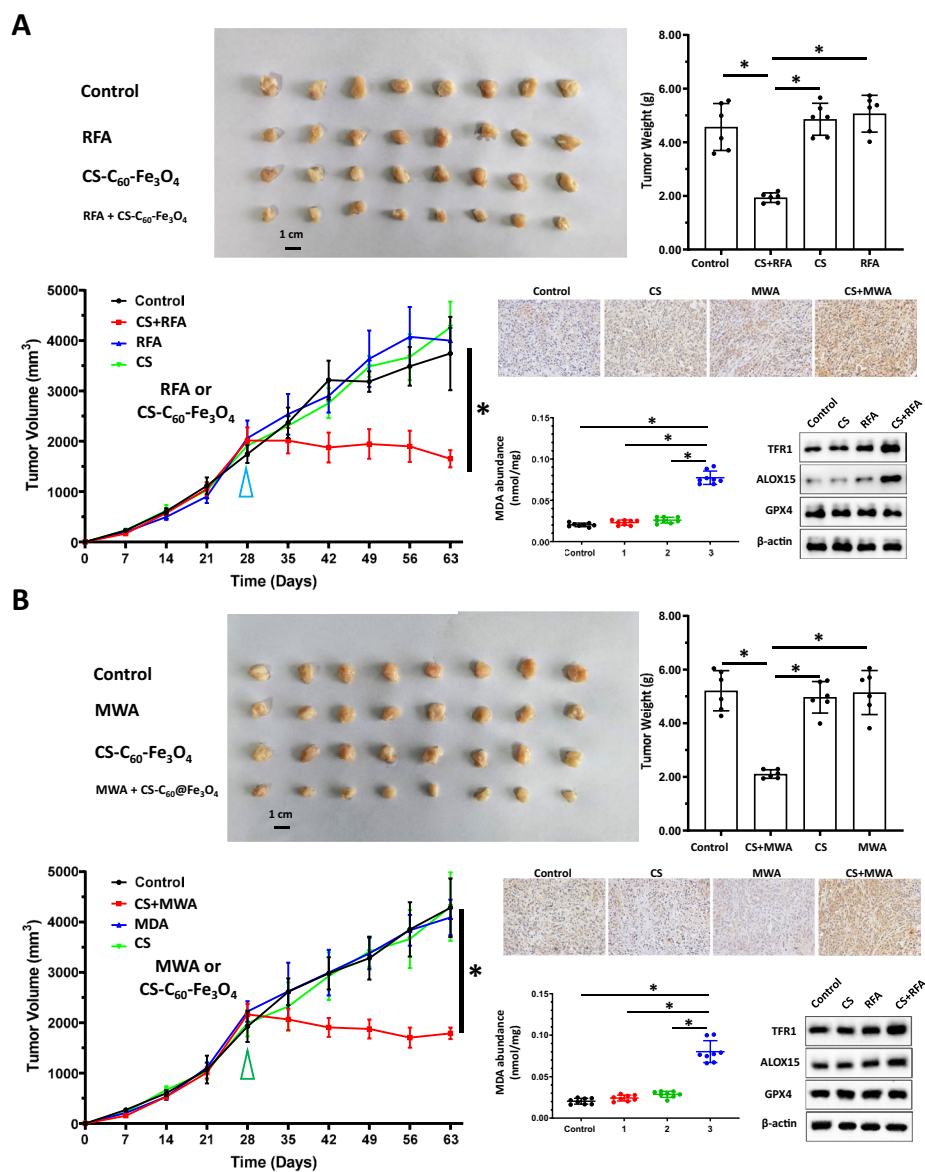
**Fig. 6** CS-C$_{60}$-Fe$_3$O$_4$ up-regulates the antitumor activity of thermal ablation on HCC tumor tissue. MHCC97-H cells were obtained in culture, and after inoculation of nude mice to form subcutaneous tumor tissue, CS-C$_{60}$-Fe$_3$O$_4$ was administered by tail vein injection and magnetic field induced C$_{60}$ enrichment in the tumor tissue followed by thermal ablation. **A** RFA; **B** MWA) (including CS-C$_{60}$-Fe$_3$O$_4$ alone or RFA and MWA alone), and thereafter periodically Tumor volumes were measured to plot tumor growth curves. Tumor weights were measured and tumor tissue samples were subjected to western blotting. The expression levels of TFR1, ALOX15, and GPX4 were examined using their respective antibodies. Actin was used as the endogenous control

ablation) (Zhu and Rhim 2019; Liu et al. 2022). Studies of molecular mechanisms have shown that incomplete ablation can act as a cellular damage/stress factor to induce cellular stress response mechanisms, such as the epithelial mesenchymal transition (EMT) and Notch pathways in HCC cells, ultimately inducing and promoting the recurrence and metastasis of HCC (Wang et al. 2022a; Ikemoto et al. 2017). Thus, the inhibition of

EMT is an important strategy for improving the antitumor therapeutic effect of thermal ablation on HCC, delaying HCC recurrence after EMT, and improving patient prognosis. Combinations of different treatment strategies can achieve more effective antitumor outcomes. For example, molecular targeted drugs can inhibit EMT in HCC cells and exert a sensitising effect on RFA (Li et al. 2021; Feng et al. 2018a). The use of immune checkpoints Inhibitors (ICIs) and transhepatic arterial chemoembolization (TACE) have been reported in combination with RFA (Anand and Acharya 2021; Fedele et al. 2022). The findings of the present study greatly expand our understanding of RFA adjuvant therapy: fullerenes have the property of expansion by heat, which is ideal for use in combination with RFA; at the same time, the use of $Fe_3O_4$ to prepare them as metal fullerenes enables their specific distribution in tumor tissues, which ultimately achieves a perfect fit with thermal ablation. It is worth mentioning that fullerenes themselves have a good safety profile and only exert a damaging effect on tumor tissues under the effect of thermal ablation, which is a great advantage. In addition, EMT is closely related to the metabolic characteristics of HCC cells (aberrant metabolism and Warburg effect) and the tumor tissue microenvironment (Yue et al. 2022; Chen et al. 2021; Mu et al. 2023). Our results showed that $CS\text{-}C_{60}\text{-}Fe_3O_4$ also interfered with the normal iron metabolism and induced ferroptosis in HCC cells under the effect of thermal ablation. Iron is essential for normal cellular physiology, and abnormalities in iron metabolism can induce cellular ferroptosis (Yue et al. 2022; Chen et al. 2021; Mu et al. 2023). In malignant tumor cells, ferroptosis is associated with abnormal glycolipid metabolism and oxidative metabolism-free radical scavenging (Tang et al. 2021; Nie et al. 2023). $CS\text{-}C_{60}\text{-}Fe_3O_4$ may interfere with normal iron metabolism in HCC cells through $Fe_3O_4$. However, the exact molecular mechanism remains to be explored in detail. In the present study, a preliminary exploration of the possible mechanism of $CS\text{-}C_{60}\text{-}Fe_3O_4$ action was performed by utilizing western blotting of HCC subcutaneous tumor tissue to detect ferroptosis-related factors. $CS\text{-}C_{60}\text{-}Fe_3O_4$ did induce the expression of TFR1 (Cai et al. 2023) and ALOX15 (Ma et al. 2022b), but not GPX4 (Lee and Roh 2023), in response to thermal ablation, suggesting that $CS\text{-}C_{60}\text{-}Fe_3O_4$ may affect iron metabolism but not lipid metabolism in HCC cells.

In addition to radiofrequency ablation, nanomaterials have also been used in radiofrequency-induced hyperthermia. These reports are mainly on gold nanocori or curcumin-coated gold nanoparticles drug-carrying particles (Rezaeian et al. 2022; Amini et al. 2017, 2018). Nanogold has good physicochemical properties and curcumin has definite antitumor activity against HCC (Rezaeian et al. 2022; Amini et al. 2017, 2018). This all shows the significance of nanomedicines in the treatment of RFA. At the same time, the new nanoparticles have improved re-physicochemical properties and tissue distribution, but their stability in vivo is also important.(Ahmadi Kamalabadi et al. 2022; Badirzadeh et al. 2022). The $CS\text{-}C_{60}\text{-}Fe_3O_4$ prepared in this study can ensure the stability during the magnetic field action cycle after administration.

Our results are also highly instructive in terms of the route of antitumor drug administration. Current routes of anti-tumor drug therapy for HCC are mainly systemic (systemic chemotherapy) and local administration. (Xie et al. 2017) Intravenous infusion of ICIs (e.g., therapeutic monoclonal antibodies to PD-1/PD-L1) or oral administration of TKIs, such as sorafenib, are considered systemic administration, whereas TACE, for example, is considered local administration. (Lee and Roh 2023) Systemic treatment/

drug administration is associated with a variety of adverse effects on the body's organs, whereas local dosing strategies, such as TACE, can cause some degree of trauma to the patient (even today's minimally invasive dosing strategies are not completely non-invasive). Therefore, magnetic targeting of drug delivery in this study is of great importance and deserves further exploration.

## Conclusion

In this study, we reported for the first time the $Fe_3O_4$-based metallofullerene CS-$C_{60}$-$Fe_3O_4$, which is capable of achieving enriched distribution in tumor tissues under magnetic field induction. CS-$C_{60}$-$Fe_3O_4$ can promote the antitumor effect of thermal ablation on HCC tissues. This study not only expands our understanding of metallofullerenes, but also provides more options for precise and safer and more effective thermal ablation therapy for HCC.

## Supplementary Information

The online version contains supplementary material available at https://doi.org/10.1186/s12645-024-00245-7.

---

**Additional file 1: Figure S1.** FTIR spectrum characteristics of CS and $C_{60}$ mixtures.We used CS and $C_{60}$ mixtures to detect the absorbance values of the samples at different UV wavelengths. The results are shown as FTIR spectrum curves.

**Additional file 2: Figure S2.** Stability assay of CS-$C_{60}$-$Fe_3O_4$ in rat serum. In order to test the stability of CS-$C_{60}$-$Fe_3O_4$ in the circulatory system in vivo, we prepared a sample of 0.5 mg/ml (0-time point) by mixing CS-$C_{60}$-$Fe_3O_4$ with rat serum (obtained from rat blood specimens and stored at 4 °C overnight to allow sufficient coagulation, and thereafter separated from serum using a high-speed centrifuge). Thereafter, the samples were incubated for 24 h (24 h-time point) at 37 °C and finally the samples from both time points were subjected to absorption detection at indicated wave-length. The results are shown as absorption curves of the samples at both time points.

**Additional file 3: Table S1.** Tissue distribution of $C_{60}$ under different conditions.

**Additional file 4: Table S2.** Tissue distribution of $C_{60}$ under different conditions.

---

### Author contributions
FF: concept, design, statistics, data collection, manuscript writing, final approval. JS, ZC, XG and FF: design, statistics, and data collection. HS and YC: data collection. XL and XZ: concept, data collection. XZ: statistics, data collection. All co-authors contributed to the article and approved the submitted version.

### Availability of data and materials
All data generated or analyzed during this study are available from the corresponding author on reasonable request.

## Declarations

### Ethics approval and consent to participate
In this study, the acquisition, preservation, and corresponding experimental protocols, designs, and techniques for the use of human-related materials (including cell lines) were reviewed and approved by the Medical Ethics Committee of the Fifth Medical Center of the Chinese People's Liberation Army General Hospital. Animal welfare and ethics related to the purchase, breeding, and experimental design were reviewed and approved by the Animal Ethics Committee of the Fifth Medical Center of the Chinese People's Liberation Army General Hospital.

### Consent for publication
Not applicable.

### Competing interests
The authors declare that they have no known competing financial interests or personal relationships that could have appeared to influence the work reported in this paper.

## References

Ahmadi Kamalabadi M, Neshastehriz A, Ghaznavi H, Amini SM (2022) Folate functionalized gold-coated magnetic nanoparticles effect in combined electroporation and radiation treatment of HPV-positive oropharyngeal cancer. Med Oncol 39(12):196. https://doi.org/10.1007/s12032-022-01780-2

Amini SM, Kharrazi S, Jaafari MR (2017) Radio frequency hyperthermia of cancerous cells with gold nanoclusters: an in vitro investigation. Gold Bull 50:43–50. https://doi.org/10.1007/s13404-016-0192-6

Amini SM, Kharrazi S, Rezayat SM, Gilani K (2018) Radiofrequency electric field hyperthermia with gold nanostructures: role of particle shape and surface chemistry. Artif Cells Nanomed Biotechnol 46(7):1452–1462. https://doi.org/10.1080/21691401.2017.1373656

Anand AC, Acharya SK (2021) New developments in the treatment of hepatocellular carcinoma: the concept of adjuvant and neoadjuvant chemotherapy. J Clin Exp Hepatol 11:284–287. https://doi.org/10.1016/j.jceh.2021.04.003

Badirzadeh A, Alipour M, Najm M, Vosoogh A, Vosoogh M, Samadian H, Hashemi AS, Farsangi ZJ, Amini SM (2022) Potential therapeutic effects of curcumin coated silver nanoparticle in the treatment of cutaneous leishmaniasis due to Leishmania major in-vitro and in a murine model. J Drug Deliv Sci Technol 74:103576

Cai S, Ding Z, Liu X, Zeng J (2023) Trabectedin induces ferroptosis via regulation of HIF-1alpha/IRP1/TFR1 and Keap1/Nrf2/GPX4 axis in non-small cell lung cancer cells. Chem Biol Interact 369:110262. https://doi.org/10.1016/j.cbi.2022.110262

Chen X, Li J, Kang R, Klionsky DJ, Tang D (2021) Ferroptosis: machinery and regulation. Autophagy 17:2054–2081. https://doi.org/10.1080/15548627.2020.1810918

Fedele M, Sgarra R, Battista S, Cerchia L, Manfioletti G (2022) The epithelial-mesenchymal transition at the crossroads between metabolism and tumor progression. Int J Mol Sci. https://doi.org/10.3390/ijms23020800

Feng F et al (2018a) Which is the best combination of TACE and Sorafenib for advanced hepatocellular carcinoma treatment? A systematic review and network meta-analysis. Pharmacol Res 135:89–101. https://doi.org/10.1016/j.phrs.2018.06.021

Feng F et al (2018b) Pregnane X receptor mediates sorafenib resistance in advanced hepatocellular carcinoma. Biochim Biophys Acta Gen Subj 1862:1017–1030. https://doi.org/10.1016/j.bbagen.2018.01.011

Forner A, Reig M, Bruix J (2018) Hepatocellular carcinoma. Lancet 391:1301–1314. https://doi.org/10.1016/S0140-6736(18)30010-2

Funasaka H, Sakurai K, Oda Y, Yamamoto K, Takahashi T (1995) Magnetic properties of Gd@C82 metallofullerene. Chem Phys Lett 232(3):273–277. https://doi.org/10.1021/jp990036h

Gallego I et al (2022) A 3D peptide-/[60]fullerene hybrid for multivalent recognition. Angew Chem Int Ed Engl 61:e202210043. https://doi.org/10.1002/anie.202210043

GBD 2019 Hepatitis B Collaborator (2022) Global, regional, and national burden of hepatitis B, 1990–2019: a systematic analysis for the Global Burden of Disease Study 2019. Lancet Gastroenterol Hepatol 7:796–829. https://doi.org/10.1016/S2468-1253(22)00124-8

Hao J et al (2023) Combination treatment with FAAH inhibitors/URB597 and ferroptosis inducers significantly decreases the growth and metastasis of renal cell carcinoma cells via the PI3K-AKT signaling pathway. Cell Death Dis 14:247. https://doi.org/10.1038/s41419-023-05779-z

Huo Y et al (2019) A temperature-sensitive phase-change hydrogel of topotecan achieves a long-term sustained antitumor effect on retinoblastoma cells. Onco Targets Ther 12:6069–6082. https://doi.org/10.2147/OTT.S214024

Ikemoto T, Shimada M, Yamada S (2017) Pathophysiology of recurrent hepatocellular carcinoma after radiofrequency ablation. Hepatol Res 47:23–30. https://doi.org/10.1111/hepr.12705

Laface C et al (2022) Targeted therapy for hepatocellular carcinoma: old and new opportunities. Cancers (basel). https://doi.org/10.3390/cancers14164028

Lee J, Roh JL (2023) Targeting GPX4 in human cancer: implications of ferroptosis induction for tackling cancer resilience. Cancer Lett 559:216119. https://doi.org/10.1016/j.canlet.2023.216119

Li B et al (2021) Rhamnetin decelerates the elimination and enhances the antitumor effect of the molecular-targeting agent sorafenib in hepatocellular carcinoma cells via the miR-148a/PXR axis. Food Funct 12:2404–2417. https://doi.org/10.1039/d0fo02270e

Li J et al (2022a) Room-temperature logic-in-memory operations in single-metallofullerene devices. Nat Mater 21:917–923. https://doi.org/10.1038/s41563-022-01309-y

Li P et al (2022b) Inhibition of cannabinoid receptor type 1 sensitizes triple-negative breast cancer cells to ferroptosis via regulating fatty acid metabolism. Cell Death Dis 13:808. https://doi.org/10.1038/s41419-022-05242-5

Liao X et al (2022) Fullerene nanoparticles for the treatment of ulcerative colitis. Sci China Life Sci 65:1146–1156. https://doi.org/10.1007/s11427-021-2001-0

Liu YY et al (2022) A novel small molecular inhibitor of DNMT1 enhances the antitumor effect of radiofrequency ablation in lung squamous cell carcinoma cells. Front Pharmacol 13:863339. https://doi.org/10.3389/fphar.2022.863339

Ma Y et al (2020) DNA methyltransferase mediates the hypermethylation of the microRNA 34a promoter and enhances the resistance of patient-derived pancreatic cancer cells to molecular targeting agents. Pharmacol Res 160:105071. https://doi.org/10.1016/j.phrs.2020.105071

Ma DB et al (2022a) A novel small-molecule inhibitor of SREBP-1 based on natural product monomers upregulates the sensitivity of lung squamous cell carcinoma cells to antitumor drugs. Front Pharmacol 13:895744. https://doi.org/10.3389/fphar.2022.895744

Ma XH et al (2022b) ALOX15-launched PUFA-phospholipids peroxidation increases the susceptibility of ferroptosis in ischemia-induced myocardial damage. Signal Transduct Target Ther 7:288. https://doi.org/10.1038/s41392-022-01090-z

Mu Y, Fan Y, He L et al (2023) Enhanced cancer immunotherapy through synergistic ferroptosis and immune checkpoint blockade using cell membrane-coated nanoparticles. Cancer Nano 14:83. https://doi.org/10.1186/s12645-023-00234-2

Nie D, Guo T, Zong X et al (2023) Induction of ferroptosis by artesunate nanoparticles is an effective therapeutic strategy for hepatocellular carcinoma. Cancer Nano 14:81. https://doi.org/10.1186/s12645-023-00232-4

Rathmell WK et al (2022) Management of metastatic clear cell renal cell carcinoma: ASCO guideline. J Clin Oncol 40:2957–2995. https://doi.org/10.1200/JCO.22.00868

Rezaeian A, Amini SM, Najafabadi MRH, Farsangi ZJ, Samadian H (2022) Plasmonic hyperthermia or radiofrequency electric field hyperthermia of cancerous cells through green-synthesized curcumin-coated gold nanoparticles. Lasers Med Sci 37(2):1333–1341. https://doi.org/10.1007/s10103-021-03399-7

Shao Z et al (2018) ETS-1 induces Sorafenib-resistance in hepatocellular carcinoma cells via regulating transcription factor activity of PXR. Pharmacol Res 135:188–200. https://doi.org/10.1016/j.phrs.2018.08.003

Sung H et al (2021) Global cancer statistics 2020: GLOBOCAN estimates of incidence and mortality worldwide for 36 cancers in 185 countries. CA Cancer J Clin 71:209–249. https://doi.org/10.3322/caac.21660

Tang D, Chen X, Kang R, Kroemer G (2021) Ferroptosis: molecular mechanisms and health implications. Cell Res 31:107–125. https://doi.org/10.1038/s41422-020-00441-1

Tanzi L, Terreni M, Zhang Y (2022) Synthesis and biological application of glyco- and peptide derivatives of fullerene C(60). Eur J Med Chem 230:114104. https://doi.org/10.1016/j.ejmech.2022.114104

The Polaris Observatory HCV Collaborators (2022) Global change in hepatitis C virus prevalence and cascade of care between 2015 and 2020: a modelling study. Lancet Gastroenterol Hepatol 7:396–415. https://doi.org/10.1016/S2468-1253(21)00472-6

Wang T, Wang C (2019) Functional metallofullerene materials and their applications in nanomedicine, magnetics, and electronics. Small 15:e1901522. https://doi.org/10.1002/smll.201901522

Wang FS, Fan JG, Zhang Z, Gao B, Wang HY (2014) The global burden of liver disease: the major impact of China. Hepatology 60:2099–2108. https://doi.org/10.1002/hep.27406

Wang JH, Zeng Z, Sun J, Chen Y, Gao X (2021) A novel small-molecule antagonist enhances the sensitivity of osteosarcoma to cabozantinib in vitro and in vivo by targeting DNMT-1 correlated with disease severity in human patients. Pharmacol Res 173:105869. https://doi.org/10.1016/j.phrs.2021.105869

Wang Z et al (2022a) Microwave ablation versus laparoscopic resection as first-line therapy for solitary 3–5-cm HCC. Hepatology 76:66–77. https://doi.org/10.1002/hep.32323

Wang T, Li H, Xu Z, Wang C (2022b) Skin anti-inflammatory activity of water-soluble fullerene nanocomposites encompassed by sodium hyaluronate. J Cosmet Dermatol 21:4016–4019. https://doi.org/10.1111/jocd.14711

Wang C et al (2022c) Silk sericin stabilized proanthocyanidins for synergetic alleviation of ulcerative colitis. Int J Biol Macromol 220:1021–1030. https://doi.org/10.1016/j.ijbiomac.2022.08.134

Xie H et al (2017) What is the best combination treatment with transarterial chemoembolization of unresectable hepatocellular carcinoma? a systematic review and network meta-analysis. Oncotarget 8:100508–100523. https://doi.org/10.18632/oncotarget.20119

Xie H et al (2018) A new apatinib microcrystal formulation enhances the effect of radiofrequency ablation treatment on hepatocellular carcinoma. Onco Targets Ther 11:3257–3265. https://doi.org/10.2147/OTT.S165000

Yamamoto K, Funasaka H, Takahashi T, Akasaka T (1994) Isolation of an ESR-active metallofullerene of La@C82. J Phys Chem 98(8):2008–2011. https://doi.org/10.1021/j100059a004

Ye L et al (2021) Antitumor activity and potential mechanism of novel fullerene derivative nanoparticles. Molecules. https://doi.org/10.3390/molecules26113252

Yue H, Gou L, Tang Z et al (2022) Construction of pH-responsive nanocarriers in combination with ferroptosis and chemotherapy for treatment of hepatocellular carcinoma. Cancer Nano 13:4. https://doi.org/10.1186/s12645-022-00111-4

Zhao F et al (2023) Fullerene-liquid-crystal-induced micrometer-scale charge-carrier diffusion in organic bulk heterojunction. Adv Mater 35:e2210463. https://doi.org/10.1002/adma.202210463

Zheng H et al (2022) Microwave ablation versus radiofrequency ablation for subcapsular hepatocellular carcinoma: a propensity score-matched study. Eur Radiol 32:4657–4666. https://doi.org/10.1007/s00330-022-08537-5

Zhu F, Rhim H (2019) Thermal ablation for hepatocellular carcinoma: what's new in 2019. Chin Clin Oncol 8:58. https://doi.org/10.21037/cco.2019.11.03

## Publisher's Note

Springer Nature remains neutral with regard to jurisdictional claims in published maps and institutional affiliations.